Scientific Research Publishing

Advances in Materials Physics and Chemistry, 2026, 16(5), 191-211
https://www.scirp.org/journal/ampc
ISSN Online: 2162-5328
ISSN Print: 2162-531X

# Modeling and Optimization of a Triple-Cation Perovskite Solar Cell for Four-Terminal Tandem Integration

**Valentin Tapsoba, Boureima Traoré, Soumaïla Ouédraogo, Issiaka Sankara, Firmin Asmane Labidi Lompo, François Zougmoré**

Département de Physique, Laboratoire de Matériaux et Environnement (LA.M.E)-UFR/SEA, Université Joseph Ki-Zerbo, Ouagadougou, Burkina Faso
Email: valentin_tapsoba@ujkz.bf, traoreboureim@gmail.com, ouedraogosoumaila1@gmail.com, sankaraissaka@gmail.com, labidilompo@gmail.com, zougfran2013@gmail.com

**How to cite this paper:** Tapsoba, V., Traoré, B., Ouédraogo, S., Sankara, I., Lompo, F.A.L. and Zougmoré, F. (2026) Modeling and Optimization of a Triple-Cation Perovskite Solar Cell for Four-Terminal Tandem Integration. *Advances in Materials Physics and Chemistry*, **16**, 191-211.
https://doi.org/10.4236/ampc.2026.165010

**Received:** January 28, 2026
**Accepted:** May 25, 2026
**Published:** May 28, 2026



## Abstract

In the context of the energy transition, triple-cation perovskite solar cells, with their tunable bandgap (≈1.6 - 1.8 eV), high efficiencies, and improved stability, are ideal candidates for top sub-cells in tandem architectures. This study presents the numerical modeling and optimization, using SCAPS-1D, of a triple-cation perovskite solar cell with the structure ITO/$SnO_2$/$Cs_{0.05}FA_{0.79}MA_{0.15}PbI_{2.45}Br_{0.55}$/Spiro-OMeTAD/Au, targeting its integration into a four-terminal (4T) tandem configuration. Calibrated against experimental data with a maximum relative error of 0.5%, the reliable model was first used to optimize absorber parameters (thickness, doping, defect density, carrier mobilities). An optimal configuration increased the power conversion efficiency from 17.56% to 24.3%. Optimization then focused on interface engineering, correcting conduction and valence band misalignments (CBO/VBO) towards optimal ranges (0 to +0.3 eV and 0 to −0.2 eV, respectively) to enhance charge extraction while suppressing recombination. Combined with a reduction of interfacial defect densities, this approach yielded major gains in open-circuit voltage (Voc), short-circuit current density (Jsc), and fill factor (FF), culminating in a maximum efficiency of 29.36%. These results confirm the strong potential of triple-cation perovskite as a top sub-cell and validate the feasibility of 4T perovskite/CIGS tandem architectures targeting efficiencies beyond 40%, pending subsequent experimental validation.

## Keywords

SCAPS-1D, Triple-Cation Perovskite, 4T Tandem Solar Cell, Simulation Optimization, Interface Engineering

## 1. Introduction

In the current context of energy transition, perovskite solar cells have emerged as one of the most promising photovoltaic technologies due to their high efficiencies, low manufacturing costs, and significant architectural flexibility. Since their first appearance in 2009, they have demonstrated remarkable progress, now achieving a certified efficiency of 26.1% for single-junction devices [1] [2]. Moreover, their tunable bandgap represents a strategic asset for surpassing the Shockley-Queisser limit [3] by facilitating their integration into tandem architectures.

Nevertheless, operational stability remains one of the major obstacles hindering the industrialization of this technology. Humidity, thermal stress, and UV radiation induce degradation mechanisms that affect both the absorber layer and the interfaces, compromising their long-term durability. This challenge is particularly critical for wide-bandgap perovskites (1.6 - 1.8 eV), which are nonetheless essential for serving as the top sub-cell in tandem configurations [4].

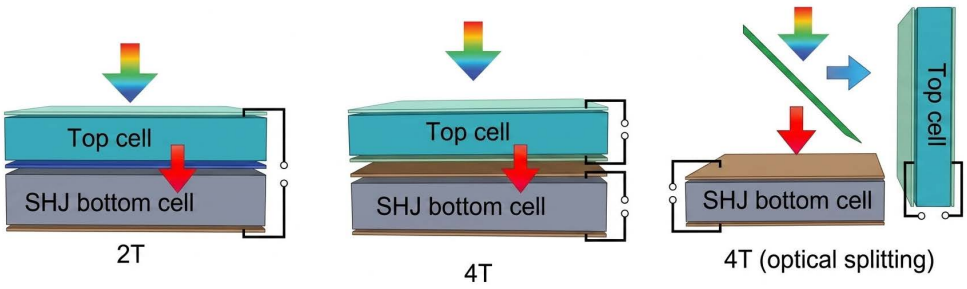


**Figure 1.** The 2T and 4T configurations of tandem solar cells [5].

Tandem solar cells are primarily categorized into two architectural types [5]: the two-terminal (2T) and four-terminal (4T) configurations, which differ in their electrical interconnection schemes and associated operational constraints (see **Figure 1**). In 2T devices, the sub-cells are connected in series, imposing a strict requirement for matching their photogenerated currents. Consequently, any current limitation in one sub-cell directly affects the overall performance, making device optimization particularly demanding. In contrast, 4T architectures rely on the complete electrical independence of the sub-cells, allowing each to operate at its individual maximum power point. This enhanced flexibility facilitates the optimization of materials and structural parameters, albeit at the cost of greater technological complexity, and is generally associated with higher efficiencies [6].

Furthermore, beyond the critical stability challenges that remain for perovskite-based solar cells especially in tandem configurations where thermal and ionic degradations continue to limit operational durability numerical simulations represent an indispensable tool for analyzing the impact of structural, optical, and electronic parameters, identifying optimal configurations, and more effectively guiding experimental efforts. Currently, the best experimental tandem devices achieve

efficiencies on the order of 30% to over 31% in various configurations [7], with realistic projections of potential efficiencies approaching or exceeding 40% depending on the materials and optimization strategies employed, particularly for well-calibrated multi-junction architectures [8] [9].

Triple-cation perovskites currently represent one of the most robust solutions for the top sub-cells of tandem cells due to their enhanced crystalline stability, improved defect tolerance, and optoelectronic properties suitable for spectral management, justifying their growing adoption in wide-bandgap tandems [10] [11].

These advantages underpin our choice for the present study, which constitutes the first part of a work dedicated to a 4T triple-cation perovskite/CIGS tandem solar cell. CIGS is a favored tandem partner due to its complementary bandgap and technological maturity. This work specifically focuses on optimizing the top triple-cation perovskite sub-cell, whose structure ITO/$SnO_2$/$Cs_{0.05}FA_{0.79}MA_{0.15}PbI_{2.45}Br_{0.55}$/Spiro-OMeTAD/Au is inspired by the single-junction experimental device by Alanazi *et al.* (2020) [12], which offers a good compromise between performance and stability.

What optimal parameters enable the perovskite sub-cell to ensure a maximum contribution within a 4T perovskite/CIGS tandem solar cell? The objective of this study is to determine, through numerical simulation, the ideal absorber and interface properties that would yield a model for a high-performance triple-cation perovskite sub-cell, perfectly integrable into a 4T tandem architecture, with the prospect of achieving a tandem efficiency exceeding 40%.

To achieve this objective, this study will investigate the influence of key absorber parameters such as thickness, doping, total defect density, and carrier mobility on the electrical performance (Jsc, Voc, FF, and PCE) of the cell. Subsequently, we will proceed to optimize the interfaces between the absorber and the charge transport layers, as these regions are recognized as critical sites for recombination and energy losses in perovskite cells [13].

## 2. Materials and Methods

### 2.1. Structure and Operation of the Studied Cell

The studied solar cell, like any other perovskite solar cell, consists of a stack of thin films deposited on a substrate, as shown in **Figure 2**. The central element of this architecture is the perovskite absorber layer, whose essential function is to capture solar radiation and generate electron-hole pairs [4]. In this study, the absorber layer is a triple-cation perovskite with the structure: $Cs_{0.05}FA_{0.79}MA_{0.15}PbI_{2.45}Br_{0.55}$. The $Cs^+$-$MA^+$-$FA^+$ mixture optimizes the lattice tolerance factor, stabilizing the cubic or tetragonal $\alpha$-phase, which is essential for efficient light absorption. $Cs^+$ reinforces the lattice rigidity and prevents the transition to non-photoactive phases (such as $\delta$-$FAPbI_3$), while $MA^+$ and $FA^+$ maintain a slightly distorted geometry favorable for carrier transport [14]-[16].

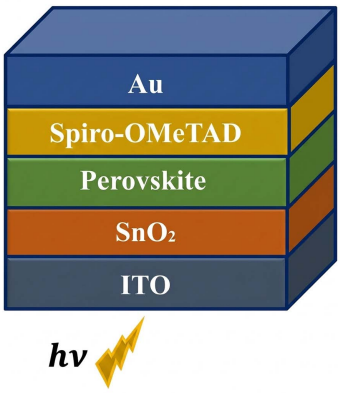


**Figure 2.** Structure of the studied cell.

The optimal operation of the perovskite sub-cell within a perovskite/CIGS architecture relies on effective spectral complementarity with the CIGS sub-cell. To this end, the perovskite bandgap must be judiciously adjusted to ensure high transparency in the near-infrared region, typically between 700 and 1200 nm, thereby allowing the transmission of photons to the underlying CIGS sub-cell [17]. Under solar illumination, the perovskite absorber enables electrons from the valence band to move to the conduction band, leaving holes behind.

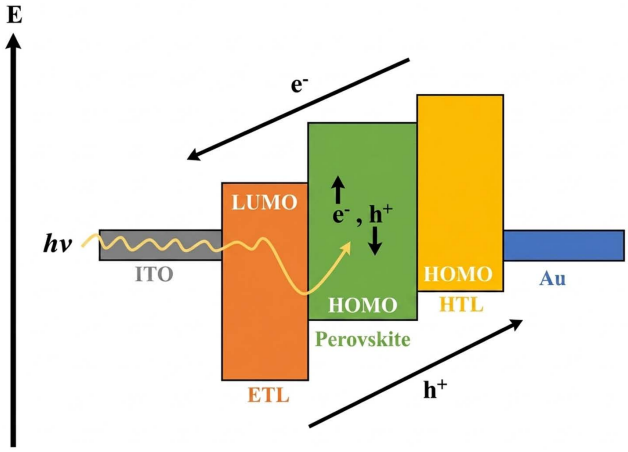


**Figure 3.** Band diagram and operational mechanism.

The generated electron-hole pair (see **Figure 3**) rapidly dissociates into free charges, as the exciton binding energy in perovskite is relatively low (a few tens of meV at room temperature) [18]. These charges must then be selectively extracted using transport layers: the electron transport layer (ETL, here $SnO_2$), which facilitates the transfer of photogenerated electrons to the electrode while acting as a barrier against their recombination with holes, and the hole transport layer (HTL, here Spiro-OMeTAD), which collects the positive charges. For these processes to be efficient, energy level alignment is crucial: the LUMO (lowest unoccupied molecular orbital) level of the ETL must be lower than that of the absorber, while the

HOMO (highest occupied molecular orbital) level of the HTL must be higher than that of the perovskite [19]-[21]. Meeting these conditions promotes selective extraction and efficient transport of charge carriers to the contact electrodes, the rear in Au and the front in ITO.

## 2.2. Numerical Model and Simulation Method

The operation of a solar cell is governed by the generation, transport, and recombination of charge carriers, processes described by Poisson's Equation (1) and the continuity equations for electrons (2) and holes (3). In this study, these equations are solved numerically using the SCAPS-1D software, which is widely recognized for modeling thin-film photovoltaic devices, particularly perovskite cells [19].

$$\frac{\mathrm{d}^2\psi(x)}{\mathrm{d}x^2} = \frac{e}{\varepsilon_0\varepsilon_r}\left[p(x) - n(x) + N_D - N_A + \rho_P + \rho_n\right] \tag{1}$$

$$\frac{\mathrm{d}}{\mathrm{d}x}J_n(x) - e\frac{\partial n(x)}{\partial t} - e\frac{\partial \rho_n}{\partial t} = G_n(x) - R_n(x) \tag{2}$$

$$\frac{\mathrm{d}}{\mathrm{d}x}J_P(x) - e\frac{\partial p(x)}{\partial t} - e\frac{\partial \rho_p}{\partial t} = G_p(x) - R_p(x) \tag{3}$$

where: $\varepsilon_0$ and $\varepsilon_r$ denote the vacuum and relative dielectric constants, respectively; $n$ and $p$ denote the free carrier concentrations (electrons and holes); $N_D$ and $N_A$ denote the donor and acceptor concentrations; $\rho_n$ and $\rho_P$ denote the charge densities of electrons and holes; $J_n$ and $J_P$ represent the electron and hole current densities; $R_n$ and $R_P$ correspond to the electron and hole recombination rates; and $G_n$ and $G_P$ represent the electron and hole generation rates.

For the numerical simulations, SCAPS-1D receives as input the numerical model of our solar cell (see **Table 1**), constructed from a critical analysis of the literature to faithfully reproduce the experimental electrical behavior reported by Alanazi *et al.* (2020) [12] with a maximum relative error set at 0.5%. This model integrates all the physical and electronic parameters of the different layers, including thicknesses, doping levels, mobilities, defect densities, electron affinities, bandgaps, etc. Based on these inputs, the software numerically solves Poisson's equation and the carrier continuity equations (see Equations (1) (2) and (3). As output, it provides the device's electrical characteristics, namely the open-circuit voltage (Voc), short-circuit current density (Jsc), fill factor (FF), power conversion efficiency (PCE), etc. The software thus provides a rigorous framework for quantitatively analyzing the influence of input parameters on the device's electrical performance.

To reconcile model accuracy with numerical feasibility, several simplifying assumptions were adopted. Interface defect densities are assumed to be constant and spatially homogeneous, while the bandgap ($E_g$) and electron affinity ($\chi$) are considered invariant. Carrier mobilities are treated as uniform and isotropic across all layers. The optical absorption process is modeled within a strictly one-dimensional framework, without accounting for scattering phenomena. The device tem-

perature is fixed at 300 K, and the illumination spectrum corresponds to the AM1.5G standard. These approximations, widely accepted in the literature, allow the analysis to focus on the dominant electrical and optical mechanisms while maintaining relevant correspondence with experimental devices [22].

**Table 1.** Numerical model of the studied cell [23]-[29].

| Layer | Spiro-OMeTAD | Perovskite | $SnO_2$ | ITO |
|---|---|---|---|---|
| **Thickness (nm)** | 200 | 500 | 20 | 50 |
| $E_g$ (eV) | 2.9 | 1.6 | 3.5 | 3.6 |
| $\chi$ (eV) | 2.2 | 3.9 | 4 | 4.3 |
| $\varepsilon_r$ ($F \cdot cm^{-1}$) | 3.06 | 6.6 | 9 | 8.9 |
| $N_C$ ($cm^{-3}$) | $2.2 \times 10^{18}$ | $10^{18}$ | $2.2 \times 10^{16}$ | $2.2 \times 10^{18}$ |
| $N_v$ ($cm^{-3}$) | $1.9 \times 10^{19}$ | $10^{18}$ | $10^{19}$ | $1.8 \times 10^{18}$ |
| $V_{th,n}$ (cm/s) | $10^7$ | $10^7$ | $10^7$ | $10^7$ |
| $V_{th,p}$ (cm/s) | $10^7$ | $10^7$ | $10^7$ | $10^7$ |
| $\mu_n$ ($cm^2/V \cdot s$) | $2.1 \times 10^{-3}$ | 2 | 20 | 10 |
| $\mu_p$ ($cm^2/V \cdot s$) | $2.16 \times 10^{-3}$ | 2 | 10 | 10 |
| $N_D$ ($cm^{-3}$) | 0 | 0 | $2.2 \times 10^{17}$ | $10^{21}$ |
| $N_A$ ($cm^{-3}$) | $2 \times 10^{19}$ | $10^{15}$ | 0 | 0 |
| $N_t$ ($cm^{-3}$) | $10^{16}$ | $5.14 \times 10^{15}$ | $10^{14}$ | $10^{14}$ |
| **Interfaces** | | | | ETL/PSC/HTL |
| **Type** | | | | Neutral |
| **Electron capture cross-section ($cm^2$)** | | | | $4 \times 10^{-18}$ |
| **Hole capture cross-section ($cm^2$)** | | | | $4 \times 10^{-18}$ |
| **Energy distribution** | | | | Single |
| **Defect level reference for Et** | | | | Above highest EV |
| **Energy relative to reference (eV)** | | | | 0.6 |
| **Total density ($cm^{-2}$)** | | | | $8 \times 10^{10}$ |

## 2.3. Validation

The validation of the numerical model for the studied solar cell is performed by comparing its electrical performance with that of the actual cell reported by Alanazi *et al.* (2020) [12] (see **Figure 4** and **Table 2**). This step ensures the simulation results remain coherent, realistic, and representative of the real behavior of the experimental device.

The comparison between experimental results and simulated data reveals a remarkable degree of agreement, confirming the robustness and reliability of the adopted numerical model. The near-perfect overlap of the current-voltage curves presented in **Figure 4** demonstrates that the simulation faithfully reproduces the experimental behavior of the cell across all operating regimes, thereby validating

the coherence of the implemented physical parameters. This qualitative observation is supported by a quantitative analysis of the photovoltaic parameters summarized in Table 2.

The use of relative error enables moving beyond a simple visual comparison to conduct a more rigorous model validation. The simulated open-circuit voltage coincides exactly with the experimental value (1.08 V), reflecting an adequate description of recombination mechanisms. Similarly, the short-circuit current and the fill factor exhibit only marginal deviations on the order of 0.13%, indicating precise modeling of carrier absorption, transport, and collection phenomena, as well as internal resistances. The simulated conversion efficiency is strictly identical to the measured value, confirming that SCAPS-1D consistently accounts for all physical processes governing the device's operation. Under these conditions, the numerical model can be considered a reliable predictive tool for the analysis and optimization of the studied solar cell.

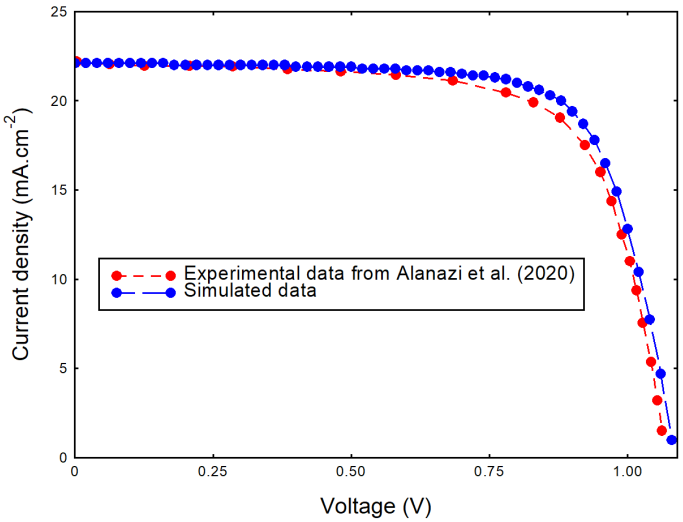


Figure 4. Experimental and simulated J-V curves.

Table 2. Experimental and simulated characteristics.

| Parameters | Voc (V) | Jsc (mA/cm²) | FF (%) | PCE (%) |
|---|---|---|---|---|
| **Experimental** | 1.08 | 22.13 | 73.19 | 17.56 |
| **Simulation** | 1.08 | 22.10 | 73.29 | 17.56 |
| **Relative Error** $\left(\frac{\lvert X_{\text{Exp.}} - X_{\text{Sim.}} \rvert}{X_{\text{Exp.}}} \times 100\right)$ | 0% | 0.13% | 0.13% | 0% |

## 3. Results and Discussion

### 3.1. Optimization of the Absorber Layer

#### 3.1.1. Influence of the Absorber Layer Thickness

Figure 5 analyzes the impact of the triple-cation perovskite absorber thickness,

ranging from 200 to 1250 nm, on the electrical performance of the studied solar cell.

The study reveals a marked dependence of photovoltaic performance on the absorber layer thickness. The power conversion efficiency (PCE, Figure 5(d)) increases continuously as the thickness increases from 200 to 1250 nm, rising from 14.40% to 18.87%. This improvement is primarily driven by the growth of the short-circuit current density (Jsc, Figure 5(b)), which increases from 16.02 to 23.93 mA·cm$^{-2}$. This trend indicates increasingly efficient photon absorption until a quasi-saturated regime is established for thicknesses above 800 - 900 nm, beyond which the current reaches a plateau.

Concurrently, the fill factor (FF, Figure 5(c)) decreases significantly, dropping from 81.51% to 70%. This degradation is attributed to the intensification of bulk recombination and the progressive deterioration of carrier transport within a larger active volume, a phenomenon accounted for in the recombination model implemented in SCAPS-1D. When the thickness exceeds the effective carrier diffusion length, charge extraction becomes less efficient.

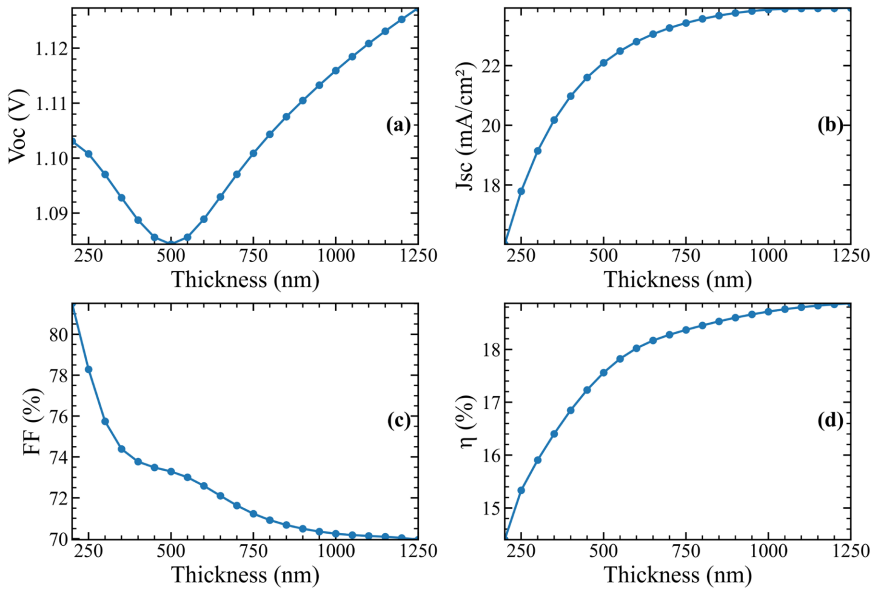


Figure 5. Variation of electrical performance as a function of absorber thickness.

The open-circuit voltage (Voc, Figure 5(a)) exhibits a non-monotonic evolution. After a slight decrease between 200 and 500 nm, it gradually increases to reach 1.13 V at 1250 nm. This U-shaped trend reflects the competition between enhanced carrier generation (favorable for Voc) and increased recombination losses (which tend to reduce it).

Although the maximum efficiency is achieved at 1250 nm, the performance saturation beyond 800 nm leads to the identification of an optimal range between 800 and 1000 nm, offering a balanced compromise between efficiency, electrical stability, and loss control. From an experimental perspective, this range is compatible with commonly used perovskite deposition techniques (e.g., multi-layer

spin-coating, blade coating, or slot-die coating), while thicknesses approaching 1250 nm present greater technological and structural challenges [30]-[32]. Consequently, the thickness is set to 1000 nm for the remainder of the study to investigate the combined influence of doping and defect density on electrical performance.

### 3.1.2. Influence of Doping and Total Defect Density

The heatmaps in Figure 6 highlight the cross-influence of the acceptor doping, varying from $10^{13}$ to $1.5 \times 10^{15}$ cm$^{-3}$, and the absorber defect density, ranging between $10^{9}$ and $10^{16}$ cm$^{-3}$, on photovoltaic performance.

The results reveal a high sensitivity of photovoltaic performance to the absorber defect density ($N_t$). For low to moderate values ($N_t \leq 10^{14}$ cm$^{-3}$), the efficiency ($\eta$, Figure 6(a)), open-circuit voltage (Voc, Figure 6(b)), and fill factor (FF, Figure 6(d)) remain high and stable, with efficiencies exceeding 24%. Conversely, when $N_t$ reaches $10^{15}$ - $10^{16}$ cm$^{-3}$, all parameters degrade significantly as a direct consequence of intensified non-radiative Shockley-Read-Hall recombination, which reduces carrier lifetime.

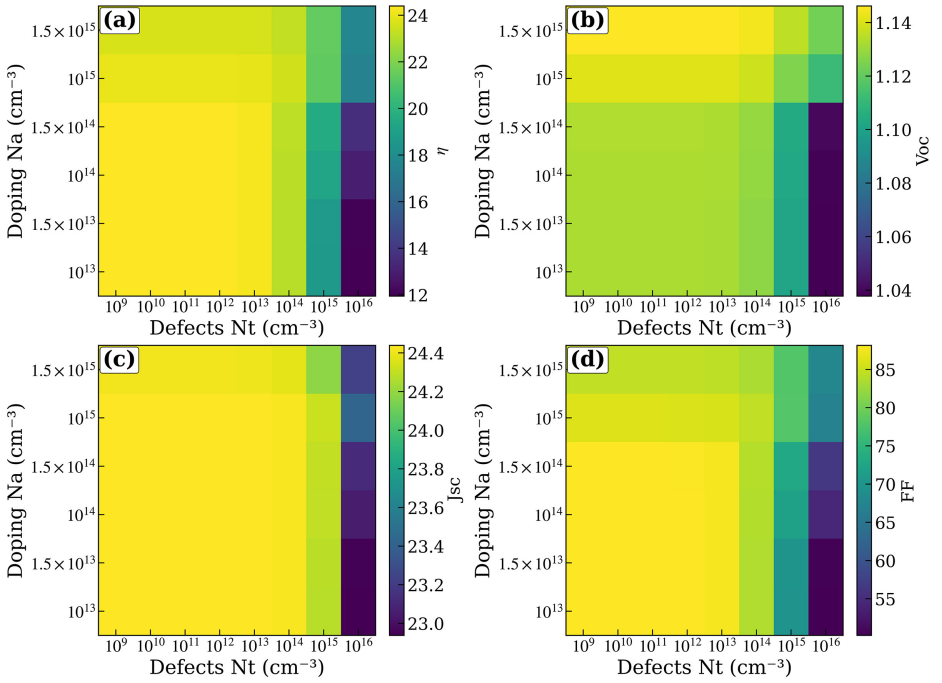


Figure 6. Variation of performance as a function of doping and total defect density.

The open-circuit voltage (Voc, Figure 6(b)) exhibits a marked dependence on acceptor doping ($N_a$) when the defect density remains low. Increasing $N_a$ strengthens the internal electric field and reduces the saturation current, thereby improving Voc. At high defect densities, this beneficial trend is radically reversed: Voc drops sharply, particularly for low doping levels, revealing the dominance of bulk recombination mechanisms. The short-circuit current density (Jsc, Figure 6(c)) remains largely insensitive to doping as long as $N_t \leq 10^{14}$ cm$^{-3}$, indicating efficient

carrier collection. However, as $N_t$ increases, Jsc decreases noticeably due to the reduced diffusion length and increasingly inefficient collection a phenomenon accentuated at low doping levels. This degradation marks a clear reversal of its initial stability.

The fill factor (FF, **Figure 6(d)**) evolves similarly to the efficiency. It retains high values for low defect densities, then deteriorates sharply at high $N_t$, under the effect of increased saturation current and recombination around the maximum power point. Even at low $N_t$, excessive doping ($N_a \gtrsim 10^{15}$ cm$^{-3}$) slightly degrades the FF, indicating an optimal compromise between doping and charge transport.

An optimal regime emerges for $N_t \leq 10^{13}$ - $10^{14}$ cm$^{-3}$ and $N_a$ between $10^{14}$ and $10^{15}$ cm$^{-3}$, enabling efficiencies close to 25% ($\eta$, **Figure 6(a)**). This optimum is consistent with the state-of-the-art for high-performance perovskites [33]. Conversely, doping levels above $10^{15}$ cm$^{-3}$ induce increased structural degradation and ionic instability, in agreement with trends observed in simulations [34]. The following section focuses, for a representative $N_t$ of $10^{13}$ cm$^{-3}$, on the joint analysis of doping and electron mobility, as the latter can become a limiting factor when dopant concentrations increase.

### 3.1.3. Influence of Doping and Carrier Mobility

**Figure 7** illustrates the combined impact of the acceptor concentration, varying from $10^{13}$ to $1.5 \times 10^{15}$ cm$^{-3}$, and the charge carrier mobility (electrons and holes), ranging between 1 and 5 cm$^2$·V$^{-1}$·s$^{-1}$, on the electrical performance of the studied solar cell.

In triple-cation perovskite solar cells, the ratio of electron to hole mobilities is generally close to unity ($\mu_n/\mu_p \approx 1$) [35]. Consequently, the simulations performed here were configured with symmetric variations of electron and hole mobilities, imposing $\mu = \mu_n = \mu_p$, in order to realistically replicate ambipolar charge transport within the absorber layer.

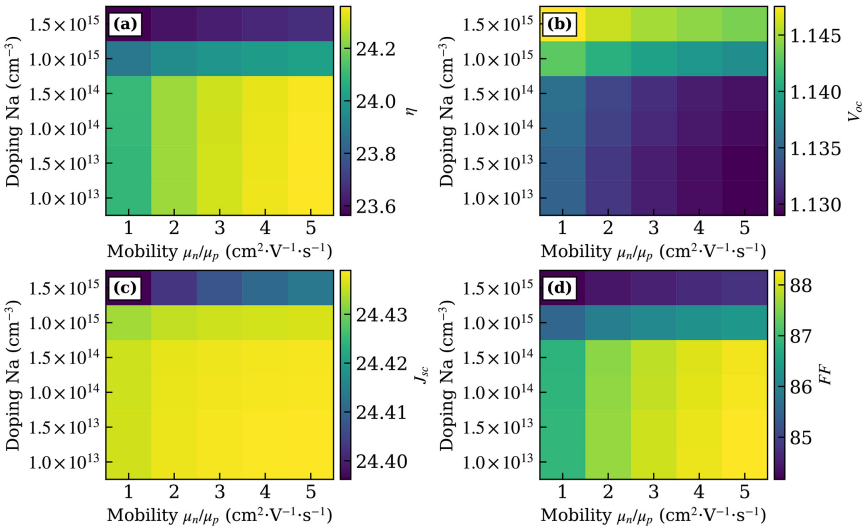


**Figure 7.** Variation of performance as a function of doping and carrier mobility.

The open-circuit voltage (Voc, Figure 7(b)) depends strongly on the acceptor concentration and increases with doping, reaching approximately 1.147 V for $N_a = 1.5 \times 10^{15}$ cm$^{-3}$. This trend is attributed to the reduction of the reverse saturation current. However, an increase in mobility induces a slight reduction in Voc, a phenomenon explained by a faster redistribution of carriers towards the interfaces, where interfacial recombination becomes predominant when interface quality is limited. The short-circuit current density (Jsc, Figure 7(c)) remains practically constant around 24.4 mA·cm$^{-2}$, indicating photon absorption close to saturation within the studied parameter domain. Concurrently, the fill factor (FF, Figure 7(d)) increases with mobility and reaches about 88% for intermediate doping levels, reflecting reduced transport losses and more efficient charge extraction, whereas excessive doping deteriorates this parameter.

Overall, an optimal operating domain is identified for acceptor concentrations on the order of $N_a \approx 10^{13}$ - $10^{14}$ cm$^{-3}$ combined with a carrier mobility $\mu \geq 3$ cm$^2$·V$^{-1}$·s$^{-1}$, enabling the concurrent optimization of the conversion efficiency $\eta$, open-circuit voltage Voc, and fill factor FF. This parameter range is fully compatible with current experimental capabilities [36] [37]. Therefore, the reference parameter set, defined by a mobility $\mu = 3$ cm$^2$·V$^{-1}$·s$^{-1}$ and a defect density $N_t = 10^{13}$ cm$^{-3}$, is adopted for the continuation of the study, which focuses on the joint optimization of doping and absorber layer thickness, aiming to identify an optimal compromise between efficient collection of photogenerated charges and the minimization of recombination losses.

### 3.1.4. Influence of Doping and Thickness

Figure 8 illustrates the combined impact of acceptor concentration ($N_a$), ranging from $10^{13}$ to $1.5 \times 10^{15}$ cm$^{-3}$, and absorber layer thickness, ranging from 200 nm to 1200 nm, on the photovoltaic performance of the studied solar cell.

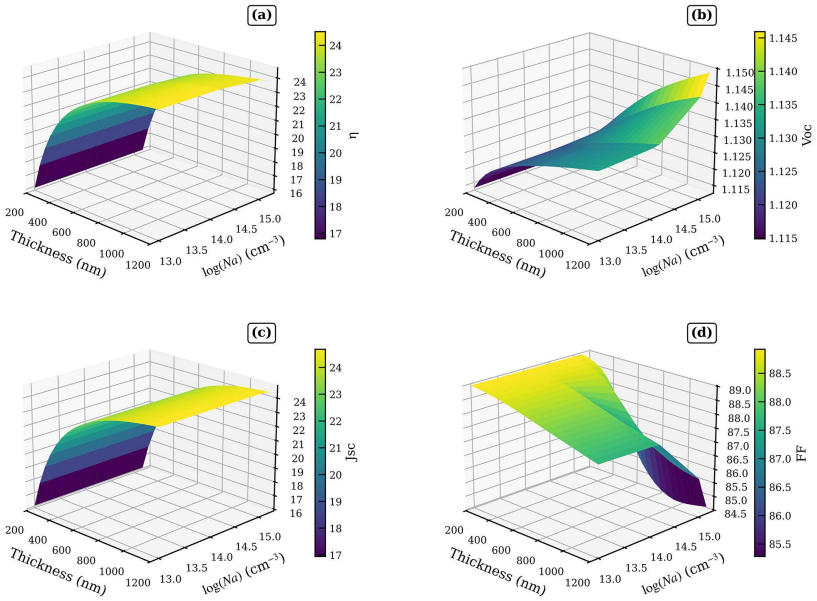


Figure 8. Variation of electrical performance as a function of doping and thickness.

The power conversion efficiency ($\eta$, Figure 8(a)) increases significantly with absorber thickness, driven directly by the increase in photogenerated current density, and then evolves more slowly at greater thicknesses, reflecting the approach of an optical saturation regime. The short-circuit current density (Jsc, Figure 8(c)) shows a rapid increase with thickness up to approximately 800 - 1000 nm, beyond which the gain becomes marginal due to the near-complete absorption of the incident spectrum. Its dependence on $N_a$ concentration remains generally weak over the considered range.

The open-circuit voltage (Voc, Figure 8(b)) increases significantly with Na, reflecting the improvement of the internal electric field and the effective reduction of recombination losses as the doping level promotes better charge separation. Voc also increases with thickness, although this dependence is less pronounced than that observed with doping. The fill factor (FF, Figure 8(d)) generally decreases as thickness increases, a behavior consistent with increased transport losses and recombinations in a thicker absorber; this degradation becomes more pronounced for high Na values, where resistive and recombination effects are intensified.

The efficiency $\eta$ thus results from a compromise between the increase in Jsc and Voc and the progressive penalty on FF. Although the maximum $\eta$ value is achieved for thicknesses near the upper limit of the studied range and for high doping levels, a value of $\eta = 24.3\%$ obtained for an absorber thickness of 1000 nm and a concentration of $N_a = 10^{14}$ cm$^{-3}$ appears as an optimal condition considering the overall device constraints. This configuration indeed offers an efficiency substantially equivalent to the maximum value while providing a better compromise in terms of operational stability, technological deposition limitations, doping control, and manufacturing cost.

The effectiveness of this approach highlights the decisive role of the absorber in improving perovskite device performance. However, despite these advances, interfaces often constitute critical zones where energy losses are concentrated, as interfacial defects and poor energy level alignment between the absorber and the charge transport layers promote non-radiative recombinations that limit the open-circuit voltage and overall conversion. The following section is therefore devoted to the analysis and optimization of these interfaces, in order to enhance their energetic alignment and limit residual interfacial recombination.

## 3.2. Optimization of Interfaces between Functional Layers

### 3.2.1. Evaluation of Functional Layer Band Alignment

Reducing recombination at the ETL/perovskite/HTL interfaces constitutes a critical lever for optimizing the extraction and collection of photogenerated charge carriers. The efficiency of this process depends directly on the band alignment, which must ensure both efficient electron injection and selective hole extraction. Thus, a valence band offset (VBO) between 0 and −0.2 eV at the HTL/perovskite interface promotes hole extraction without creating a limiting barrier, while a

conduction band offset (CBO) from 0 to +0.3 eV between the ETL and the perovskite constitutes a moderate "spike," suitable for blocking recombination while allowing efficient electron collection [38]. The analytical expressions for these energy offsets are recalled below:

$$\mathrm{VBO} = \left(\chi_{HTL} + E_{g,HTL} - \chi_{abs} - E_{g,abs}\right) \tag{4}$$

$$\mathrm{CBO} = \left(\chi_{abs} - \chi_{ETL}\right) \tag{5}$$

where $\chi_{HTL}$ and $\chi_{ETL}$ denote the electron affinities of the hole transport layer (HTL) and electron transport layer (ETL), respectively, $\chi_{abs}$ that of the perovskite absorber, and $E_g$ the bandgap of each material.

Based on the parameters considered in this study, the estimated VBO yields a value of −0.40 eV. Such a valence band offset, significantly below the optimal limit of −0.2 eV, corresponds to a pronounced cliff at the HTL/perovskite interface. While this cliff may facilitate hole transfer to some extent, it simultaneously increases the probability of interfacial recombination via deep states located near this interface. An excessively negative VBO typically leads to a decrease in Voc and a deterioration of the HTL's selectivity, which reduces the overall cell efficiency [39].

Similarly, the calculated conduction band offset yields CBO = −0.1 eV. This negative value indicates the presence of a cliff at the ETL/perovskite interface, inducing a collection barrier likely to favor electron recombination, particularly under strong illumination. Although a moderate cliff (≈−0.1 eV) still allows acceptable electron transport, it remains detrimental for maximizing Voc and reducing resistive losses associated with interfacial transfer [39].

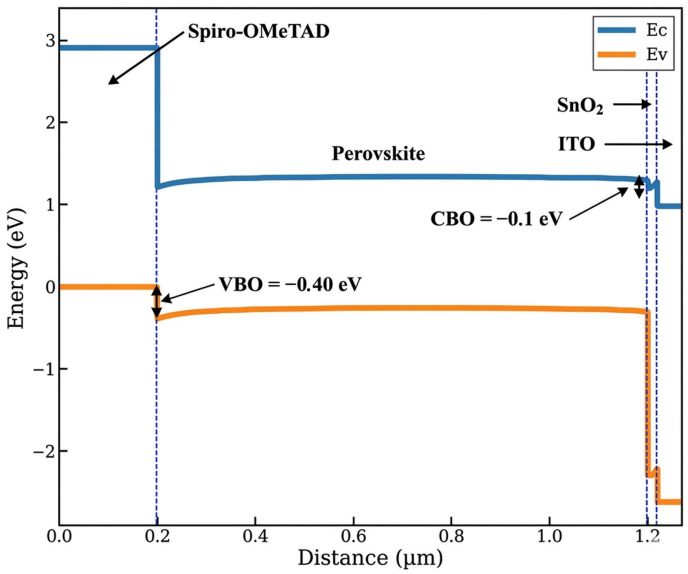


**Figure 9.** Energy band diagram of the studied solar cell.

Figure 9 highlights that the cell's performance is primarily limited by poor energetic alignment at the interfaces. At the $SnO_2$/perovskite interface, the negative

CBO (≈−0.1 eV) creates an electron cliff that promotes electron accumulation and increases interfacial recombination, directly penalizing the open-circuit voltage [40]. At the perovskite/Spiro-OMeTAD interface, the strongly negative VBO (≈−0.40 eV) corresponds to a pronounced valence band cliff, reducing the hole contact selectivity and intensifying recombination losses, with a simultaneous degradation of Voc and the fill factor.

The quasi-flat bands within the bulk of the perovskite confirm that the limitations are dominated by interfaces rather than bulk transport. Therefore, performance optimization requires a controlled repositioning of the CBO towards [0; +0.3] eV and the VBO towards [0; −0.2] eV, a prerequisite for reducing recombination and maximizing device efficiency [41].

### 3.2.2. Optimization of the CBO via the $SnO_2$ Layer

The previous analysis highlighted a negative CBO (≈−0.1 eV) at the ETL/perovskite interface. To optimize the band alignment, a parametric study was conducted by varying the electron affinity of $SnO_2$ (3.8 - 4.0 eV) and of the absorber (3.85 - 4.1 eV), the effects of which on the cell performance are presented in **Figure 10**.

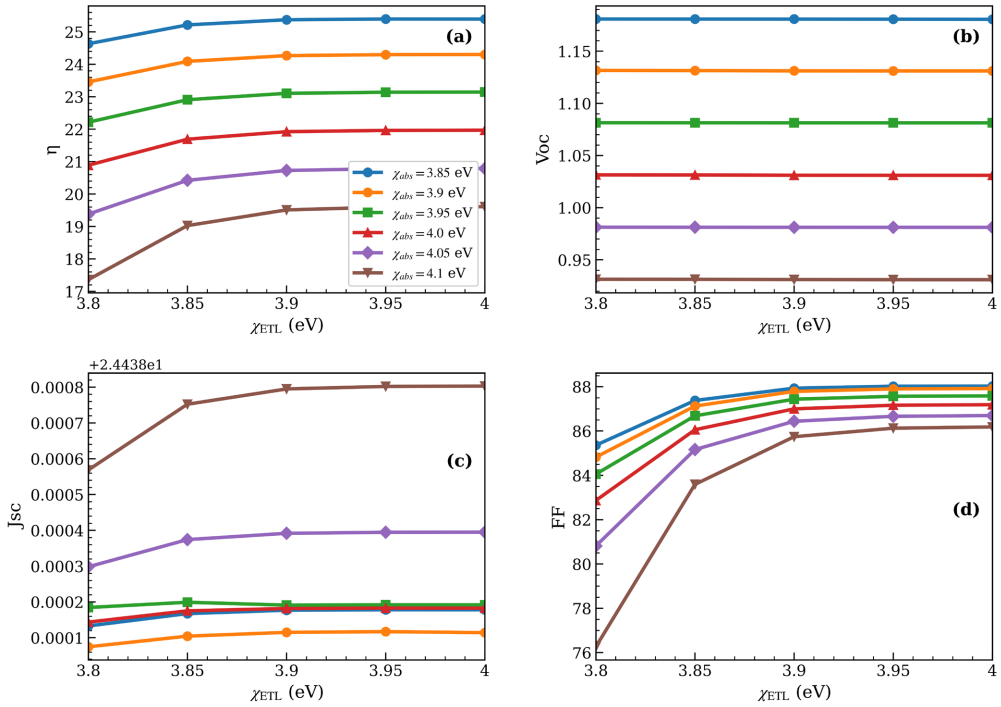


**Figure 10.** Simulation of the influence of the electron affinity of the $SnO_2$ layer and that of the absorber on the electrical performance of the perovskite solar cell.

The open-circuit voltage (Voc) remains largely independent of $\chi_{ETL}$ but decreases sharply with increasing $\chi_{abs}$ (from 1.16 V to 0.93 V), worsening the negative CBO (≈−0.1 eV) and promoting interfacial recombination. The short-circuit current (Jsc) increases significantly with $\chi_{abs}$, while the influence of $\chi_{ETL}$ is mar-

ginal, indicating better electron extraction. The fill factor (FF) is mainly controlled by $\chi_{ETL}$: it improves rapidly from 3.9 eV onward, reaching an optimal plateau of 86% - 88%. The overall efficiency ($\eta$) results from a trade-off between these parameters. It increases slightly with $\chi_{ETL}$ but decreases strongly with $\chi_{abs}$, dropping from 25% to 19%. Thus, the global optimum is achieved for $\chi_{abs} \approx 3.85$ - 3.9 eV and $\chi_{ETL} \approx 3.9$ - 4.0 eV, leading to CBO values between −0.15 eV and 0 eV.

However, considering the experimental constraints related to material stability and the reproducibility of deposition processes, a pragmatic choice is to set $\chi_{abs} \approx$ 3.9 eV and $\chi_{ETL} \approx 4.0$ eV (CBO ≈ −0.1 eV). This configuration, validated by the observed trends, will serve as the basis for the remainder of the study, which is dedicated to optimizing the valence band offset (VBO) through engineering of the Spiro-OMeTAD hole transport layer.

### 3.2.3. Optimization of the VBO via the Spiro-OMeTAD Layer

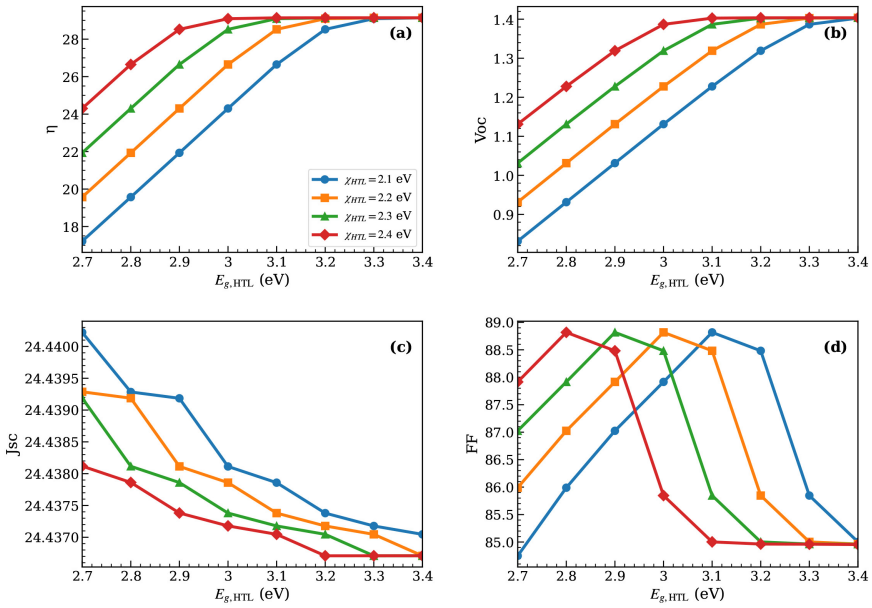


**Figure 11.** Simulation of the influence of the HTL bandgap and its electron affinity on the electrical performance of the perovskite solar cell.

The analysis is based on Equation (4), considering a perovskite characterized by $\chi_{abs} = 3.9$ eV and $E_{g,abs} = 1.6$ eV. A dual parametric sweep of the HTL's electron affinity ($\chi_{HTL}$ from 2.1 to 2.4 eV) and its optical bandgap ($E_{g,HTL}$ from 2.7 to 3.4 eV) is performed to identify configurations satisfying the optimal energy condition of $-0.2 \leq$ VBO $\leq 0$ eV. This approach allows delineation of an interfacial stability zone ensuring efficient hole extraction while limiting recombination. The complete set of results is presented in **Figure 11**.

The open-circuit voltage (Voc) increases monotonically with the HTL bandgap ($E_{g,HTL}$), reaching a plateau around 1.4 V for high values (≈3.2 - 3.4 eV). This trend reflects a reduction in interfacial recombination due to improved valence band alignment. A higher HTL electron affinity ($\chi_{HTL}$) also improves Voc by limiting

electron leakage.

The short-circuit current (Jsc) remains globally stable, as it is mainly governed by generation and transport within the perovskite. However, a slight decrease appears at high bandgaps, caused by an increased hole extraction barrier. The effect of $\chi_{HTL}$ on Jsc is marginal.

The fill factor (FF) exhibits a non-monotonic behavior, with an optimum at intermediate bandgaps (≈2.9 - 3.1 eV), reflecting a trade-off between selectivity and ease of hole extraction. Bandgaps that are too low increase recombination, while those that are too high raise the series resistance.

The efficiency ($\eta$) is maximized for $\chi_{HTL} \approx 2.3$ - 2.4 eV and $E_{g,HTL} \approx 3.1$ - 3.2 eV, where band alignment is optimal. The remainder of the study will focus on interface passivation by fixing $\chi_{HTL} = 2.4$ eV and $E_{g,HTL} = 3.1$ eV. Figure 12 confirms the significant reduction of the VBO (from an initial −0.40 eV) at the perovskite/Spiro-OMeTAD interface, promoting hole extraction. The CBO at the perovskite/$SnO_2$ interface remains unchanged at −0.1 eV, a value considered as a slight, beneficial spike. The performance gain therefore arises essentially from the optimization of the perovskite/Spiro-OMeTAD interface.

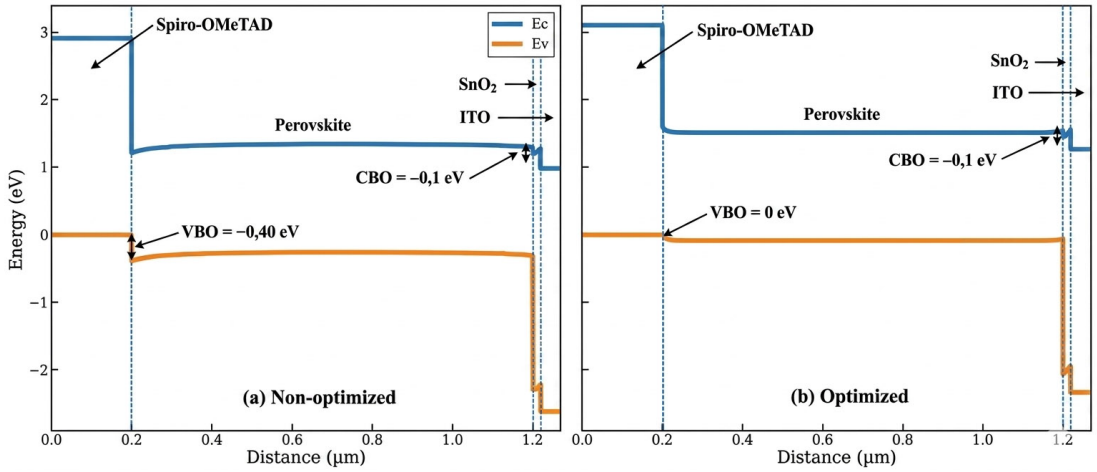


**Figure 12.** Energy band diagrams of the studied solar cell before and after optimization.

### 3.2.4. Optimization via Interface Passivation of the Solar Cell

Figure 13 highlights the critical influence of interfacial defect density on the performance of the perovskite solar cell, revealing a marked asymmetry between the ETL/perovskite and perovskite/HTL interfaces.

Voc remains stable at 1.40 V up to $10^{11}$ $cm^{-2}$ at the $SnO_2$/Perovskite interface, then drops sharply to 1.18 V at $10^{14}$ $cm^{-2}$. At the Perovskite/Spiro-OMeTAD interface, it decreases only moderately to 1.33 V, showing much better tolerance on the HTL side.

Jsc remains nearly constant (24.425 $mA/cm^2$) for the HTL interface, while it decreases slightly above $10^{12}$ $cm^{-2}$ on the ETL side. The fill factor (FF) exhibits opposite behaviors: it collapses to 82% for $SnO_2$/Perovskite at high defect densi-

ties, but increases to 89% for Spiro-OMeTAD.

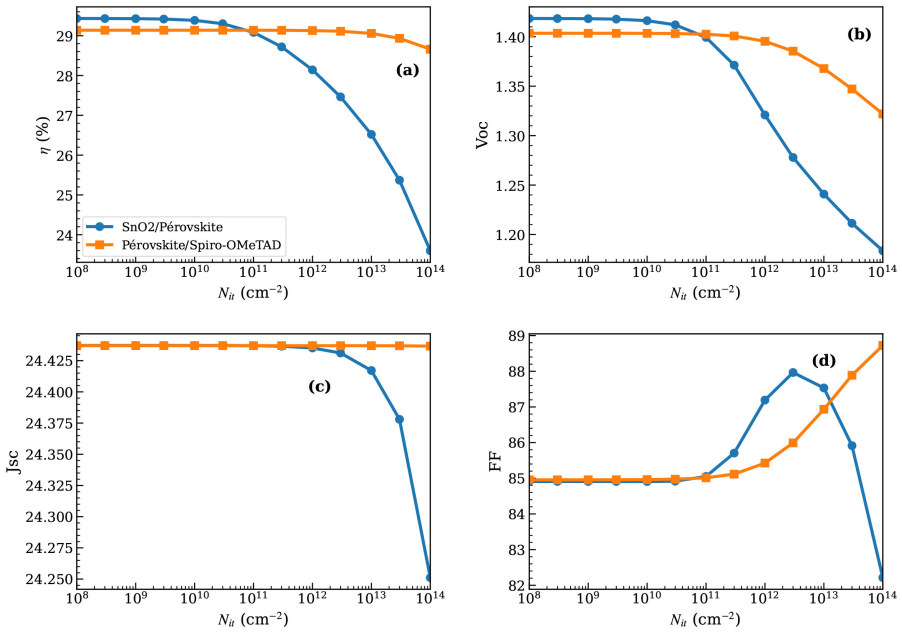


**Figure 13.** Simulation of the influence of interface defect density on the electrical performance of the perovskite solar cell.

Finally, the overall efficiency $\eta$ is strongly degraded by defects at the $SnO_2$/perovskite interface: it drops from 29.5% to only 23.5% when the defect density exceeds $10^{11}$ cm$^{-2}$, whereas it remains close to 29% for the interface with the HTL, even at $10^{13}$ cm$^{-2}$. By adopting Nit (ETL/perovskite) = $10^{10}$ cm$^{-2}$ and Nit (perovskite/HTL) = $10^{12}$ cm$^{-2}$, the electrical parameters obtained, presented in **Table 3**, show a complete and substantial improvement in the performance of the triple-cation perovskite cell after optimization. The power conversion efficiency increases from 17.56% to 29.37%, corresponding to a relative improvement of 67.25%.

**Table 3.** Experimental and simulated characteristics.

| Parameters | Voc (V) | Jsc (mA/cm²) | FF (%) | PCE (%) |
|---|---|---|---|---|
| **Initial** | 1.08 | 22.10 | 73.30 | 17.56 |
| **Optimized** | 1.40 | 24.43 | 85.51 | 29.37 |
| **Relative Improvement** $\left(\frac{\lvert X_{\text{Opt.}} - X_{\text{Ini.}}\rvert}{X_{\text{Ini.}}} \times 100\right)$ | 29.62% | 10.54% | 16.65% | 67.25% |

## 4. Conclusions and Perspectives

This study has demonstrated the potential of SCAPS-1D numerical modeling as a reliable predictive tool for identifying and optimizing the limiting mechanisms of a triple-cation perovskite solar cell, with rigorous validation (discrepancy < 0.5%)

against a reference experimental device. Systematic optimization of the absorber enabled the definition of an optimal configuration, improving efficiency from 17.56% to 24.3% through enhanced absorption and charge collection. However, the decisive improvement lever resided in interface engineering. Correcting the initial energy misalignments (negative CBO, overly negative VBO) towards optimal ranges, coupled with a reduction of interfacial defect densities, succeeded in suppressing non-radiative recombinations and strengthening contact selectivity. This approach generated substantial gains in Voc, Jsc, and FF, leading to a maximum simulated efficiency of 29.37%.

These performances, combined with the material's tunable bandgap (~1.6 eV), unequivocally confirm the relevance of triple-cation perovskite as a high-performance top sub-cell. The achieved efficiency is fully compatible with the requirements of a 4T perovskite/CIGS tandem architecture targeting an overall efficiency exceeding 40%, assuming a high-performance bottom CIGS sub-cell. However, this study presents certain inherent limitations of the 1D modeling framework, such as the assumed homogeneity of parameters and the simplification of optical phenomena. The perspectives of this work therefore lie in its experimental validation: the fabrication and characterization of the perovskite sub-cell with the optimized parameters, followed by its integration and testing in the complete tandem device with the CIGS cell. This step will be crucial for confirming the technological feasibility and operational stability of this promising architecture.

## Conflicts of Interest

The authors declare no conflicts of interest regarding the publication of this paper.

## References

[1] Kojima, A., Teshima, K., Shirai, Y. and Miyasaka, T. (2009) Organometal Halide Perovskites as Visible-Light Sensitizers for Photovoltaic Cells. *Journal of the American Chemical Society*, **131**, 6050-6051. https://doi.org/10.1021/ja809598r

[2] NREL (2024) Interactive Best Research-Cell Efficiency Chart. https://www.nrel.gov/pv/interactive-cell-efficiency.html

[3] Nazir, S., Ali, A., Aftab, A., Muqeet, H.A., Mirsaeidi, S. and Zhang, J. (2023) Techno-economic and Environmental Perspectives of Solar Cell Technologies: A Comprehensive Review. *Energies*, **16**, Article No. 4959. https://doi.org/10.3390/en16134959

[4] Afre, R.A. and Pugliese, D. (2024) Perovskite Solar Cells: A Review of the Latest Advances in Materials, Fabrication Techniques, and Stability Enhancement Strategies. *Micromachines*, **15**, Article No. 192. https://doi.org/10.3390/mi15020192

[5] Li, X., Xu, Q., Yan, L., Ren, C., Shi, B., Wang, P., *et al.* (2021) Silicon Heterojunction-based Tandem Solar Cells: Past, Status, and Future Prospects. *Nanophotonics*, **10**, 2001-2022. https://doi.org/10.1515/nanoph-2021-0034

[6] Rafiq, M., Li, H. and Yang, J. (2024) Four-Terminal Perovskite Tandem Solar Cells. *iEnergy*, **3**, 216-241. https://doi.org/10.23919/ien.2024.0025

[7] Pradhan, S., Fogat, O., Singh Shaktawat, Y., Kumar, V. and Sahu, S.K. (2025) Design, Simulation, and Optimization of Perovskite-Silicon Tandem Solar Cells. 2025 *International Conference on Recent Advances in Electrical, Electronics, Ubiquitous Com-*

*munication*, *and Computational Intelligence* (*RAEEUCCI*), Chennai, 23-25 April 2025, 1-7. https://doi.org/10.1109/raeeucci63961.2025.11048270

[8] Huang, J. and Mao, L. (2025) A Review on Perovskite/Silicon Tandem Solar Cells: Current Status and Future Challenges. *Energies*, **18**, Article No. 4327. https://doi.org/10.3390/en18164327

[9] Salah, M.M., Zekry, A., Abouelatta, M., Shaker, A., Mousa, M., Amer, F.Z., *et al.* (2022) High-Efficiency Electron Transport Layer-Free Perovskite/GeTe Tandem Solar Cell: Numerical Simulation. *Crystals*, **12**, Article No. 878. https://doi.org/10.3390/cryst12070878

[10] Li, Y., Liu, Z., Yao, K. and Jen, A.K. (2025) Perovskite-Based Tandem Solar Cells toward Commercial Application. *Advanced Energy Materials*, **16**, e03826. https://doi.org/10.1002/aenm.202503826

[11] Zhai, J.X., Xie, L. and Shafian, S. (2025) Advancements in Perovskite/CIGS Tandem Solar Cells: Material Synergies, Device Configurations, and Economic Viability for Sustainable Energy. *Nanotechnology Reviews*, **14**, Article ID: 20250196. https://doi.org/10.1515/ntrev-2025-0196

[12] Alanazi, T.I., Game, O.S., Smith, J.A., Kilbride, R.C., Greenland, C., Jayaprakash, R., *et al.* (2020) Potassium Iodide Reduces the Stability of Triple-Cation Perovskite Solar Cells. *RSC Advances*, **10**, 40341-40350. https://doi.org/10.1039/d0ra07107b

[13] Wolff, C.M., Caprioglio, P., Stolterfoht, M. and Neher, D. (2019) Nonradiative Recombination in Perovskite Solar Cells: The Role of Interfaces. *Advanced Materials*, **31**, Article ID: 1902762. https://doi.org/10.1002/adma.201902762

[14] Dipta, S.S., Howlader, A.H., Tarique, W.B. and Uddin, A. (2024) Comparative Analysis of the Stability and Performance of Double-, Triple-, and Quadruple-Cation Perovskite Solar Cells for Rooftop and Indoor Applications. *Molecules*, **29**, Article No. 2758. https://doi.org/10.3390/molecules29122758

[15] Rehman, W., McMeekin, D.P., Patel, J.B., Milot, R.L., Johnston, M.B., Snaith, H.J., *et al.* (2017) Photovoltaic Mixed-Cation Lead Mixed-Halide Perovskites: Links between Crystallinity, Photo-Stability and Electronic Properties. *Energy & Environmental Science*, **10**, 361-369. https://doi.org/10.1039/c6ee03014a

[16] Yi, C., Luo, J., Meloni, S., Boziki, A., Ashari-Astani, N., Grätzel, C., *et al.* (2016) Entropic Stabilization of Mixed A-Cation $ABX_3$ Metal Halide Perovskites for High Performance Perovskite Solar Cells. *Energy & Environmental Science*, **9**, 656-662. https://doi.org/10.1039/c5ee03255e

[17] Zhang, Y., Tang, Z., Zhang, Z., Tang, J., Li, M., Zhu, S., *et al.* (2024) Non-Destructive Buffer Enabling Near-Infrared-Transparent Inverted Inorganic Perovskite Solar Cells toward 1400 H Light-Soaking Stable Perovskite/Cu(In,Ga)$Se_2$ Tandem Solar Cells. *Journal of Energy Chemistry*, **97**, 622-629. https://doi.org/10.1016/j.jechem.2024.06.019

[18] Negi, W. and Thakur, R. (2025) Advances in Monolithic Perovskite CIGS Tandem Solar Cells: A Path to High-Efficiency Photovoltaics. *International Journal for Research in Applied Science and Engineering Technology*, **13**, 139-151. https://doi.org/10.22214/ijraset.2025.66228

[19] Norddin, N., Shafie, S., Idris, M.I., Liu, X., Lawal, I., Rummaja, M.I.D.M., *et al.* (2023). Performance Comparison of Different Electron Transport Layer for Perovskite Solar Cell with NiO as Hole Transport Layer Using SCAPS 1D. 2023 *IEEE 8th International Conference on Recent Advances and Innovations in Engineering* (*ICRAIE*), Kuala Lumpur, 2-3 December 2023, 1-6. https://doi.org/10.1109/icraie59459.2023.10468532

[20] Procel, P., Knobbe, J., Rezaei, N., Zardetto, V., Phung, N., Ma, M., *et al.* (2024) Opto-electrical Modelling and Roadmap for 2T Monolithic Perovskite/CIGS Tandem Solar Cells. *Solar Energy Materials and Solar Cells*, **274**, Article ID: 112975. https://doi.org/10.1016/j.solmat.2024.112975

[21] Sharif, R., Khalid, A., Ahmad, S.W., Rehman, A., Qutab, H.G., Akhtar, H.H., *et al.* (2023) A Comprehensive Review of the Current Progresses and Material Advances in Perovskite Solar Cells. *Nanoscale Advances*, **5**, 3803-3833. https://doi.org/10.1039/d3na00319a

[22] Alanazi, T.I. and Eid, O.I. (2023) Simulation of Triple-Cation Perovskite Solar Cells: Key Design Factors for Efficiency Promotion. *Energies*, **16**, Article No. 2717. https://doi.org/10.3390/en16062717

[23] Dipta, S.S., Uddin, A. and Conibeer, G. (2022) Enhanced Light Management and Optimization of Perovskite Solar Cells Incorporating Wavelength Dependent Reflectance Modeling. *Heliyon*, **8**, e11380. https://doi.org/10.1016/j.heliyon.2022.e11380

[24] Hossain, M.K., Arnab, A.A., Das, R.C., Hossain, K.M., Rubel, M.H.K., Rahman, M.F., *et al.* (2022) Combined DFT, SCAPS-1D, and wxAMPS Frameworks for Design Optimization of Efficient $Cs_2BiAgI_6$-Based Perovskite Solar Cells with Different Charge Transport Layers. *RSC Advances*, **12**, 34850-34873. https://doi.org/10.1039/d2ra06734j

[25] Izadi, F., Ghobadi, A., Gharaati, A., Minbashi, M. and Hajjiah, A. (2021) Effect of Interface Defects on High Efficient Perovskite Solar Cells. *Optik*, **227**, Article ID: 166061. https://doi.org/10.1016/j.ijleo.2020.166061

[26] Mohandes, A., Moradi, M. and Kanani, M. (2023) Numerical Analysis of High Performance Perovskite Solar Cells with Stacked ETLs/C60 Using SCAPS-1D Device Simulator. *Optical and Quantum Electronics*, **55**, Article No. 533. https://doi.org/10.1007/s11082-023-04778-w

[27] Peng, Z., Wei, Q., Chen, H., Liu, Y., Wang, F., *et al.* (2020) $Cs_{0.15}FA_{0.85}PbI_3/Cs_xFA_{1-x}PbI_3$ Core/Shell Heterostructure for Highly Stable and Efficient Perovskite Solar Cells. *Cell Reports Physical Science*, **1**, Article ID: 100224. https://doi.org/10.1016/j.xcrp.2020.100224

[28] Tiwari, P., Alotaibi, M.F., Al-Hadeethi, Y., Srivastava, V., Arkook, B., Sadanand, S., *et al.* (2022) Design and Simulation of Efficient SnS-Based Solar Cell Using Spiro-OMeTAD as Hole Transport Layer. *Nanomaterials*, **12**, Article No. 2506. https://doi.org/10.3390/nano12142506

[29] Tarekuzzaman, M. and Utsho, K.I.F. (2025) Advancing Solar Energy with $Cs_2TlAsI_6$ Double Halide Perovskite: A Simulation-Driven Approach for High-Efficiency Solar Cell. *Advanced Electronic Materials*, **11**, e00312. https://doi.org/10.1002/aelm.202500312

[30] Ahn, J.W., Kim, S.Y., Jeon, S.W., Oh, O.J., Lee, S.M., Park, J.H., *et al.* (2025) Ethanol-assisted Green-Solvent-Based Strategy for Slot-Die Coated Perovskite Solar Cells with over 70% Eco-Friendly Solvent Content. *Small*, **21**, e10529. https://doi.org/10.1002/smll.202510529

[31] Liu, Z., He, D., Yu, Y., Liu, X., Shai, X. and Chen, J. (2025) Slot-Die Coating Deposition Method in High-Performance Perovskite Solar Modules. *Solar RRL*, **9**, Article ID: 2400824. https://doi.org/10.1002/solr.202400824

[32] Qi, Y., Zhang, Q., Aguinaga, J., Qiu, C., Hang, R., He, S., *et al.* (2025) Engineering Inorganic Perovskite Films by $x$ Values of $DMAPbI_x$ toward Large Area Photovoltaic Devices by Slot-Die Coating. *Small*, **21**, e2503825. https://doi.org/10.1002/smll.202503825

[33] Zhou, T., Huang, X., Yao, R., Zhang, D., Liu, W. and Li, X. (2025) Integrative Enhancement of Energy-Level Alignment and Defect Passivation for High-Performance Lead-Free Perovskite Solar Cells. *Advanced Theory and Simulations*, **8**, Article ID: 2401064. https://doi.org/10.1002/adts.202401064

[34] Zhang, H., Gao, C., He, L., Zhang, D., Su, H., Liu, H., *et al.* (2025) Gradient Doping Strategy for Sn-Pb Mixed Perovskite Solar Cells with High Efficiency and Stability. *Small Methods*, **9**, Article ID: 2500064. https://doi.org/10.1002/smtd.202500064

[35] Savenije, T., Zhao, J., Liu, X., Ibrahim, B., Thieme, J., van der Poll, L., *et al.* (2024). Interplay between Structure and Charge Carrier Dynamics in CsMAFA-Based Perovskites. *Proceedings of the International Conference on Hybrid and Organic Photovoltaics*, València, 12-15 May 2024. https://doi.org/10.29363/nanoge.hopv.2024.041

[36] Heydarian, M., Loukeris, G., Bivour, M., Messmer, C., Heydarian, M., Fischer, O., *et al.* (2025) Indium-Free Recombination Layer for Perovskite-Based Multijunction-Solar-Cells- with Improved Performance Using Sputtered Zinc Tin Oxide. *Small*, **21**, e11646. https://doi.org/10.1002/smll.202511646

[37] Mann, D.S., Singh, J., Thakur, S., Kwon, S., Jeong, K. and Na, S. (2025) Influence of Fluorine Doping on Hole Transport Properties of $NiO_x$ for High-Efficiency Perovskite Solar Cells. *Solar RRL*, **9**, Article ID: 2500152. https://doi.org/10.1002/solr.202500152

[38] Salah, M.M., Zekry, A., Shaker, A., Abouelatta, M., Mousa, M. and Saeed, A. (2022) Investigation of Electron Transport Material-Free Perovskite/CIGS Tandem Solar Cell. *Energies*, **15**, Article No. 6326. https://doi.org/10.3390/en15176326

[39] He, Y., Hou, Y., Zhang, C., Jiang, L., Guo, X., Li, S., *et al.* (2025) Synergistic Optimization of Band Alignment and Defects in $CsPbI_2Br$ Perovskite Solar Cells via SCAPS-1D Simulation: Achieving > 20% Efficiency. *Solar RRL*, **9**, e202500549. https://doi.org/10.1002/solr.202500549

[40] Talukdar, A., Debnath, P., Sarkar, J. and Chatterjee, S. (2024) Unveiling the Role of Band Offset in Inorganic $RbGeI_3$-Based Perovskite Solar Cells: A Numerical Study in SCAPS-1D. *Indian Journal of Physics*, **98**, 3913-3929. https://doi.org/10.1007/s12648-024-03158-8

[41] Liu, W., Zhou, T., Chu, L. and Li, X. (2026) Band Engineering and Recombination Mechanisms in Lead-Free Perovskite Solar Cells. *Chinese Physics B*, **35**, Article ID: 028801. https://doi.org/10.1088/1674-1056/ae156b